(Received 28 April 2024, Accepted 9 July 2024, Scheduled 20 July 2024)

Compact Dual-Band Antenna Based on Dual-Cap Metasurface

Xue Chen[1, *] and Haipeng Dou[2]

[1] Department of Physics, Taiyuan Normal University, Shanxi 030619, China
[2] School of Information Engineering, Shanxi Vocational University of Engineering Science and Technology, Shanxi 030619, China

ABSTRACT: A novel compact dual-band antenna based on dual-cap metasurface (MS) is proposed. By etching circumferential circular ring slots on one side of the substrate and a large cruciform slot on the other side, the dual-cap MS operates in two frequency bands. In addition, by placing the dual-cap MS at the back of a circular ring planar antenna which serves as a reflector, the impedance characteristic of the antenna in lower band and gain both in two bands are improved. The results show that this dual-cap MS antenna operates in the Wireless Local Area Network (WLAN) bands of 2.43–2.6 GHz and 5.48–6.05 GHz. Moreover, the maximum gains in lower and upper bands can reach 6.9 and 5.8 dBi, respectively.

1. INTRODUCTION

Recently, metasurface (MS) has been widely used in the design of antennas for performance improvement in some aspects, such as increasing the gain, reducing the radar cross section, improving the bandwidth, controlling the radiation beam, and reducing the size of the antenna. In [1], a low-profile circularly polarized antenna based on MS was proposed. By employing Hilbert fractal MS, a good front-to-back ratio of the antenna was realized. In [2], by introducing the MS composed of a rectangular patch artificial magnetic conductor, a slot antenna got lower radar cross section. In [3], as a reflector, the dual-cap mushroom-like MS with a shorting via was placed at the back of a circular-polarization reconfigurable antenna to improve its impedance bandwidth and gain. In [4], a wideband antenna with the bandwidth of 33.1% was realized by using a nonuniform tapered MS structure. In [5], an antenna array with hybrid MS was proposed. By combining the ordinary rectangular patch MS and the MS with a shorting pin, the cross-polarization levels of the antenna array were suppressed. In [6], by rotating the semi-circular MS placed atop of a patch antenna, the reconfiguration of radiation pattern was achieved. In [7], an antenna based on 2-bit digital coding MS was proposed. By performing convolution operations on the coding antenna, the radiation waves could be manipulated. In [8], a gradient MS based on geometric phase theory was used to customize the radiation angle of the leaky-wave antennas and reduce the total antenna size.

A common feature of the MS antennas mentioned in [1–8] was that they all work in a single frequency band. In order to improve the performance of a dual-band antenna, MSs with dual band operation were proposed. In [9], the MS composed of pairs of nonuniform cut wires was used to reduce the mutual couplings at two independent bands of two coupled MIMO antennas. In [10], a periodic homogeneous array of split ring resonators was used to form a modulated MS, which realized the beam reconfiguration at 1.8 and 2.6 GHz. In [11], a dual-band MS based slot antenna was proposed. The MS with 4×4 square patches was used to reduce the mutual coupling for antenna system. In [12], an inhomogeneous MS was proposed to achieve the electromagnetic transparent performance of the base station antenna. In [13] and [14], the dual-band MSs with L-shape gap and non-identical arc shape were proposed to convert linearly polarized wave into circularly polarized wave, respectively. To achieve dual-band performance, an MS composed of 4×4 square patches was placed above the dipole antenna in [15]. In [16], single negative metamaterial was utilized to improve the antenna radiation characteristics for LTE 46/WLAN and Ka-band applications. In [17–19], several artificial magnetic conductor (AMC) planes were loaded separately in the wearable textile dual-band antennas, which could reduce the backward radiation of the antennas and improve the gain. Here, the MSs mentioned above both had the large dimensions.

In this paper, a compact dual-band antenna for WLAN-band (2.4 GHz and 5.8 GHz) operations is proposed. It consists of a circular ring planar radiator and a dual-cap MS. The proposed MS is called dual-cap MS because each unit has a square patch etched circumferential circular ring slots (PCCRS) on one side of the substrate and a large cruciform slot (LCS) on the other side. By introducing LCS and PCCRS, dual-band operation is provided. Furthermore, by using a dual-cap MS as a reflector, better impedance matching in lower band and higher gain of the antenna both in two bands are achieved. Meanwhile, the antenna realizes a compact layout of $0.32\lambda_0 \times 0.21\lambda_0 \times 0.11\lambda_0$ (λ_0 is the wavelength at 2.47 GHz). The measured results show that the impedance bandwidths ($|S_{11}| < -10$ dB) of the proposed MS antenna in lower and upper bands are from 2.43 to 2.6 GHz and 5.48 to 6.05 GHz, respectively. In addition, the gains over these two frequency bands are higher than 4.2 and 3.7 dBi, respectively.

2. DUAL-CAP MS UNIT

The operating frequency for a antenna loaded with MS based on given dielectric material is inversely proportional to the effec-

* Corresponding author: Xue Chen (xuechen0100@sina.com).

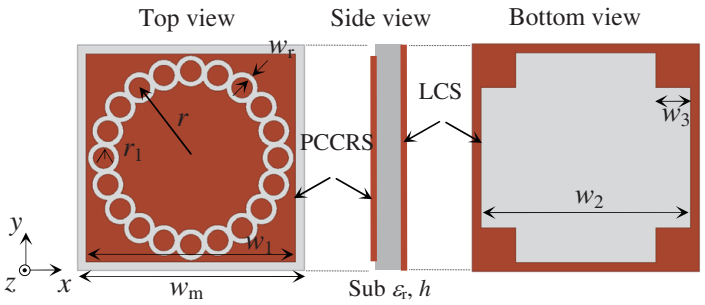

FIGURE 1. Configuration of the dual-cap MS unit.

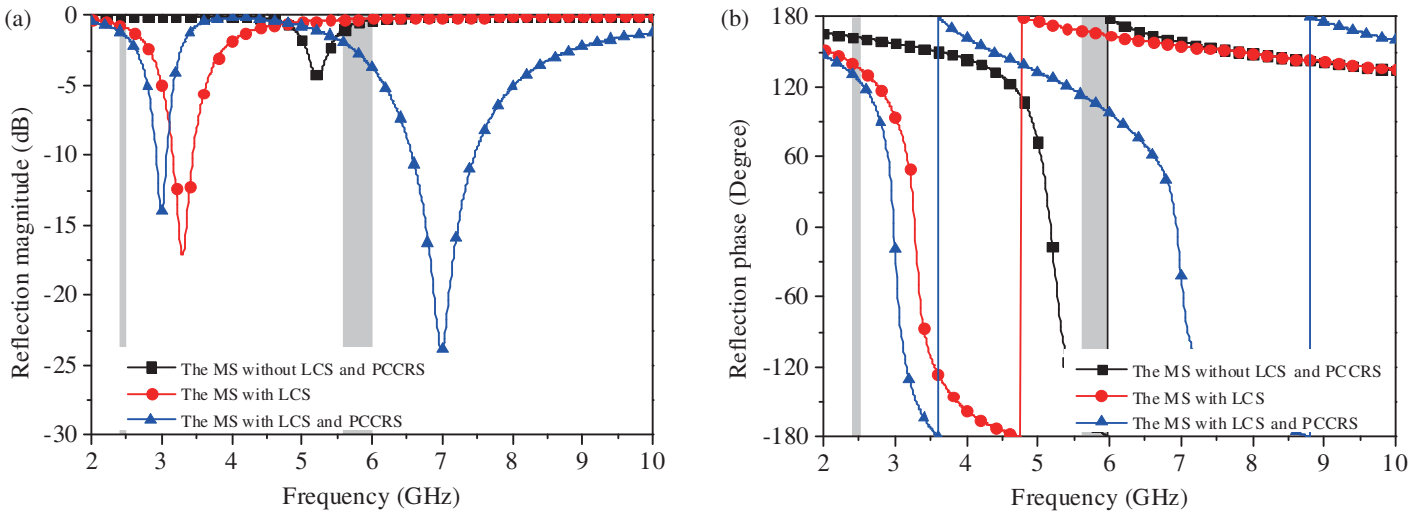

FIGURE 2. (a) Reflection magnitude and (b) phase of the MS unit.

tive permittivity and permeability. Accordingly, the Compact Factor (CF), which is the profile ratio of the antenna with MS to that without MS is given by [20]

$$CF = \frac{\varepsilon_r}{|\varepsilon_{eff}\mu_{eff}|} \tag{1}$$

where ε_{eff} and μ_{eff} are the effective permittivity and permeability of the MS, respectively. To achieve the miniaturization of antenna, CF needs to be less than 1. Thus, it is necessary to design an MS with high $\varepsilon_{eff} \times \mu_{eff}$.

Based on this, a dual-cap MS unit is proposed in this paper. Fig. 1 gives its structure. A square patch of $w_1 \times w_1$ with circumferential circular ring slots (PCCRSs) is printed on the top side of a 0.8 mm thick FR4-epoxy substrate ($\varepsilon_r = 4.4$, $\tan\delta = 0.02$). These circular ring slots are connected end to end and distributed in a circle with a radius of r. On the bottom side of the substrate, a large cruciform slot (LCS) with a width of w_2 is etched on the square metal patch. The width of the MS is calculated according to the formula:

$$w_m = \frac{c}{2f_r\sqrt{\varepsilon_r}} \tag{2}$$

where f_r and c are the resonant frequency (5.2 GHz) and the speed of light in vacuum, respectively. Also, when the perimeter of the etched slot on the MS is a guided wavelength, the resonance is easily excited. Here, the parameters of the MS unit are optimized as follows: $w_m = 13$ mm, $w_r = 0.2$ mm, $w_1 = 12$ mm, $w_2 = 12$ mm, $w_3 = 2$ mm, $r = 5$ mm and $r_1 = 0.7$ mm.

For characterization and design, the reflection magnitude and phase of the MS unit is plotted in Fig. 2. For the MS only with a rectangular patch (without LCS and PCCRS), only one operating band is formed at 5.22 GHz, as shown in Fig. 2(a). Also, in Fig. 2(b), it can be seen that the reflection phase at this frequency is close to 0°. After the LCS is introduced, since the length of LCS is designed as $4 \times w_2$ which is around a guided wavelength at 3.3 GHz, the operating band shifts down to this frequency. It indicates that the LCS is the basis of realizing the compact antenna.

When both the LCS and PCCRS are introduced, another operating band is formed at 7 GHz, and the MS has two operating frequency bands. This is because the inner perimeter of the circumferential ring slots is designed around a guided wavelength corresponding to 7 GHz. It can be seen that in the range of 2.43–2.52 GHz (as the first gray shaded area shown), the reflection magnitude is larger than −1.6 dB, and the reflection phase is about 125°. On the other hand, the reflection magnitude and phase are larger than −3.5 dB and 100° in the range of 5.6–5.98 GHz (as the second gray shaded area shown), respectively. This indicates that most of the EM waves are reflected

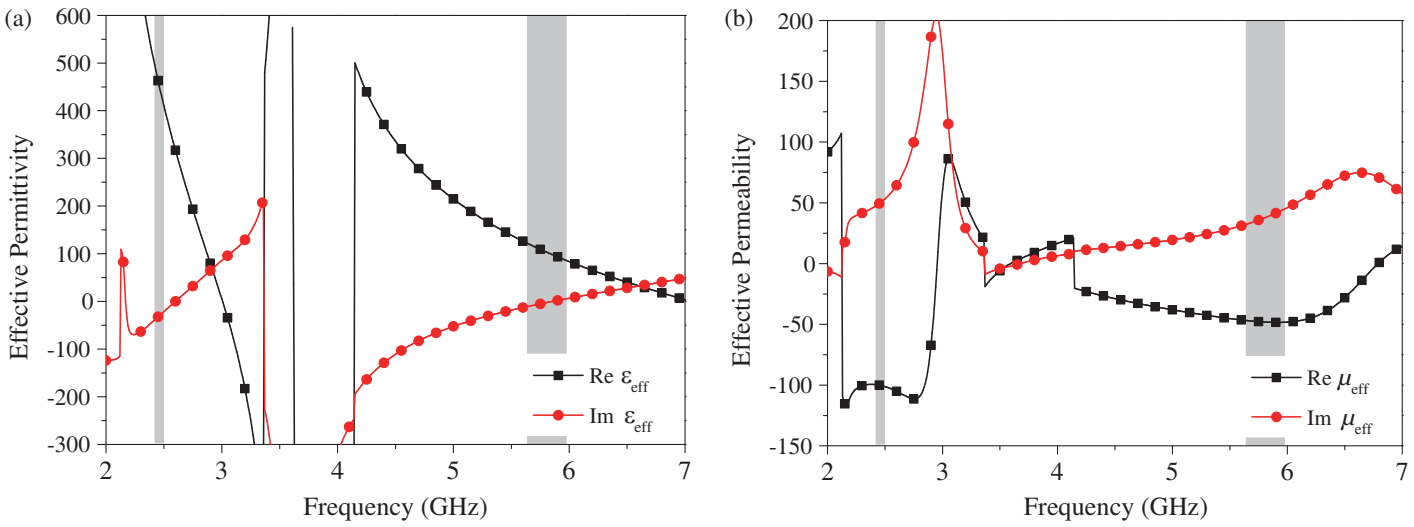

FIGURE 3. (a) Effective permittivity and (b) permeability of the MS unit.

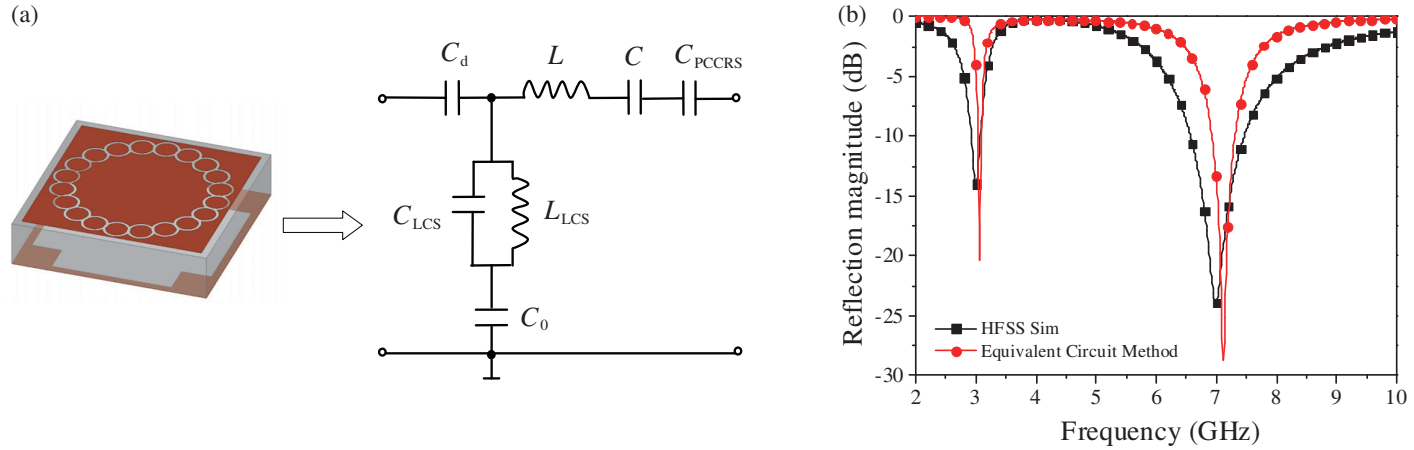

FIGURE 4. (a) Equivalent circuit of the dual-cap MS unit and (b) reflection magnitude simulated using HFSS and calculated from the equivalent circuit.

by the dual-cap MS. It exhibits a PEC-like response in these two frequency bands.

Moreover, to verify the miniaturization effect of the dual-cap MS unit, its effective permittivity (ε_{eff}) and permeability (μ_{eff}) are obtained from a full-wave parameter extracting technique, respectively [21]. The relationship between the impedance z and the S parameters is determined by

$$z = \pm\sqrt{\frac{(1+S_{11})^2 - S_{21}^2}{(1-S_{11})^2 - S_{21}^2}} \tag{3}$$

The refractive index n can be calculated according to the formula:

$$Re\,(n) = \pm\mathrm{Re}\left\{\frac{cos^{-1}\{\frac{1}{2S_{21}}\left[1-\left(S_{11}^2-S_{21}^2\right)\right]\}}{k_0 h}\right\} \tag{4}$$

$$Im\,(n) = \pm\mathrm{Im}\left\{\frac{cos^{-1}\{\frac{1}{2S_{21}}\left[1-\left(S_{11}^2-S_{21}^2\right)\right]\}}{k_0 h}\right\} \tag{5}$$

where k is the wavenumber of the incident wave in free space and h is the thickness of the substrate. Then, the ε_{eff} and μ_{eff} are directly calculated from

$$\varepsilon_{eff} = n/z \tag{6}$$

$$\mu_{eff} = nz \tag{7}$$

Figure 3 plots the effective permittivity and permeability of the dual-cap MS unit. It can be seen that the real part of ε_{eff} is positive, and that of μ_{eff} is negative in the ranges of 2.43–2.52 GHz and 5.6–5.98 GHz, which indicates that the MS unit is a single-negative medium. Also, according to the values of ε_{eff} and μ_{eff}, a very small CF can be obtained at these two bands. It indicates that the dual-cap MS unit is suitable for miniaturization design of antenna.

In addition, to further explore the working mechanism, the equivalent circuit of the dual-cap MS unit is established as shown in Fig. 4. The MS unit without LCS and PCCRS can be modeled by a parallel resonant tank, which is composed of an

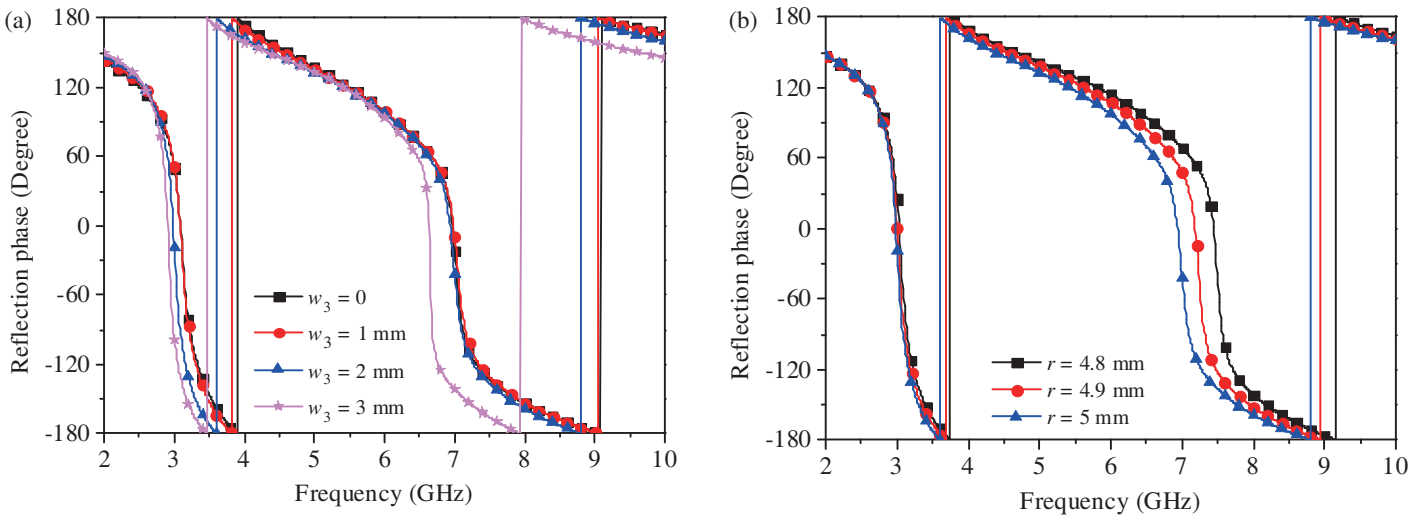

FIGURE 5. Simulated reflection phase of the MS unit (a) for different w_3, (b) for different r.

inductor L, a capacitor C, and a parallel capacitor C_0. The slot between the rectangular patches on adjacent MS units can be equivalent to a series capacitor C_d. Additional inductor L_{LCS} and capacitor C_{LCS} are introduced in the parallel branch when the LCS is loaded on the MS. Meanwhile, an additional capacitor C_{PCCRS} is added in the series branch when the PCCRS is introduced. For the optimized dual-cap MS unit, the values of the components in the equivalent circuit are assumed as follows: $L = 11.5$ nH, $C = 0.12$ pF, $C_0 = 1.27$ pF, $C_d = 0.1$ pF, $L_{LCS} = 12.1$ nH, $C_{LCS} = 0.045$ pF, and $C_{pccrs} = 0.2$ pF. Fig. 4 also shows the reflection magnitude of the dual-cap MS unit simulated using HFSS and calculated from the equivalent circuit. It can be seen that the calculated reflection magnitude is in agreement with the simulated result.

Next, the influence of w_3 and r on the reflection phase of the MS unit is studied. Fig. 5(a) shows the reflection phase of the MS unit for different w_3. When w_3 is 0 mm, the frequencies corresponding to zero reflection phases are 3.09 and 6.97 GHz, respectively. When w_3 increases to 1 mm, it has a similar performance in these two frequency bands. This indicates that there is no effect on the reflection phase when w_3 is small. However, when w_3 increases to 2 mm, the frequency corresponding to zero reflection phases in the lower band shifts down to 2.98 GHz, and the one in the upper band remains unchanged. Compared to this, with the further increase of w_3, the frequencies in both the operating bands shift down.

Figure 5(b) shows the reflection phase for different r. It can be seen that with the decrease of r, there is little effect on the reflection phase in the lower band. However, the frequency corresponding to the reflection phase of 0° in the upper band shifts up. When r decreases from 5 to 4.8 mm, the frequency increases from 6.94 to 7.44 GHz. It indicates that the frequency ratio of these dual bands can be adjusted by varying r.

3. DUAL-BAND ANTENNA BASED ON DUAL-CAP MS

Figure 6 shows the configuration of the proposed antenna based on a dual-cap MS. A circular ring planar (CRP) antenna using a noncomplete ground plane ($w \times l_g$ mm^2) is selected as the source radiator, and the dual-cap MS is placed at a distance of d ($0.09\lambda_0$ at 2.47 GHz) from the back of the source radiator, as shown in Fig. 6(a). The dual-cap MS and CRP source radiator together form a CRP MS antenna. FR4-epoxy ($\varepsilon_r = 4.4$, $\tan\delta = 0.02$, $h = 0.8$ mm) is used as both MS substrate and CRP radiator substrate, which are marked as Sub1 and Sub2, respectively. Fig. 6(b) shows the top view of the CRP radiator. It is composed of a microstrip feed line and a circular ring with a radius of r_2. In order to reduce the size of the antenna and ensure consistency with the MS array, the top of the circular ring is cut flat, and a rectangular split ring stripline is embedded to form a closed metal strip with it. Also, a rectangular stub with a length of l_2 is introduced at the bottom of the circular ring, which can extend the current path of the antenna and improve impedance matching in the upper band. Fig. 6(c) shows the top view of MS. It is composed of six PCCRSs forming a 2×3 array. Fig. 6(d) shows the bottom view of MS. It consists of six LCS units which are arranged in a 2×3 array, and the size is $w \times l$ mm^2. Table 1 lists the dimensions of the CRP MS antenna which are optimized using the Ansoft HFSS.

TABLE 1. The structural parameters of the CRP MS antenna (Unit: mm).

l	w	r	r_1	r_2	w_m	w_r	w_1	w_2	w_3
39	26	5	0.7	12	13	0.2	12	12	2
w_4	w_5	w_6	w_7	l_1	l_2	l_3	l_g	h	d
0.5	1	8	0.8	16	5.2	6.2	18	0.8	11.4

To further demonstrate the relationship between the selection of the antenna size and the resonant frequency, Fig. 7 plots the simulated current distribution on the CRP at 2.47 and 5.82 GHz, respectively. Usually, the antenna parameter can be calculated according to the formula:

$$L_m = \frac{n}{2}\lambda = \frac{nc}{2f_r\sqrt{\varepsilon_r}}, \quad n = 1, 2, 3, \cdots \tag{8}$$

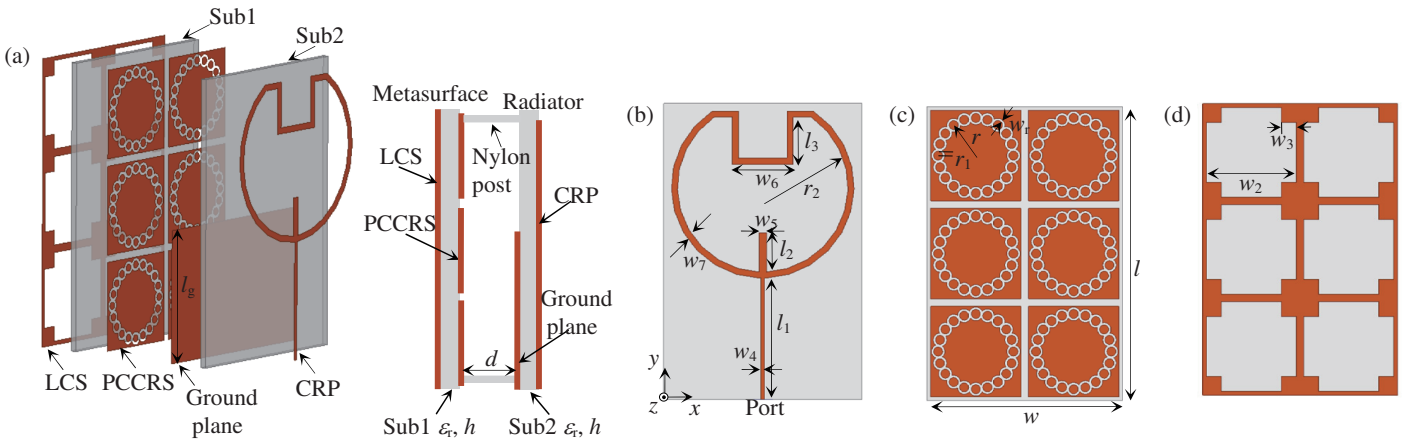

FIGURE 6. Configuration of the CRP MS antenna: (a) side view, (b) top view of the radiator, (c) top view of MS, and (d) bottom view of MS.

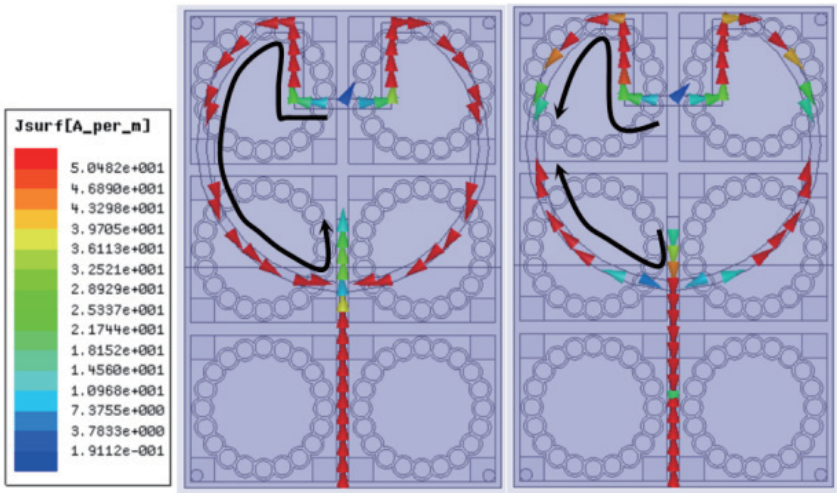

FIGURE 7. Simulated current distribution on the CRP at 2.47 and 5.82 GHz.

where L_m and λ are the current path length and guided wavelength of the corresponding resonant band, respectively. According (8), when $n = 2$, the corresponding values of L_m are 57.8 and 24.5 mm at 2.47 and 5.82 GHz, respectively. In Fig. 7, it can be seen that the lengths of the current concentration distribution (as the black arrow shown) are approximately 53 mm and 24 mm at these two operating bands, respectively. The values are nearly identical to those calculated using (8).

3.1. Improvement of the Antenna Performance

In this part, the effect of the dual-cap MS on the impedance characteristic and gain of the CRP MS antenna is studied. Firstly, the simulated input impedance and reflection coefficient $|S_{11}|$ of the antennas are given in Figs. 8(a) and (b), respectively. As an excitation source, two different modes can be excited at 2.63 and 5.82 GHz on the CRP, respectively. When the MS has not been introduced, as shown in Fig. 8(a), the input impedance of the antenna is about $50+j0\Omega$ at 5.82 GHz. Therefore, an operating band ($|S_{11}| < -10$ dB) of 5.59–5.98 GHz can be observed as shown in Fig. 8(b). Nevertheless, the input impedance at 2.63 GHz is about $150 + j50\Omega$, which has deviated from $50 + j0\Omega$. Thus, a poor impedance matching is achieved around this frequency band, and the $|S_{11}|$ is larger than -5.4 dB.

Then, the dual-cap MS is arranged as shown in Fig. 8(a), and the input impedance of the antenna is reduced to $50 + j0\Omega$ at about 2.47 GHz. This is because the lower operating band of MS is also near this frequency. This gives rise to the additional capacitance effect, and a parallel resonance appears near this frequency. In this case, a better impedance matching of the antenna in the lower band is achieved. The $|S_{11}|$ at 2.47 GHz decreases to -29 dB, and an operating band ($|S_{11}| < -10$ dB) of 2.43–2.52 GHz is observed. For this frequency band, the antenna achieves a compact electrical dimension of $0.32\lambda_0 \times 0.21\lambda_0 \times 0.11\lambda_0$ (λ_0 is the wavelength at 2.47 GHz). On the other hand, after the dual-cap MS is introduced, it has a similar impedance characteristic to the CRP antenna without MS in the upper band. This is because the MS is arranged at a distance of 11.4 mm (about $0.1\lambda_0$ at 2.47 GHz in the lower band) from the

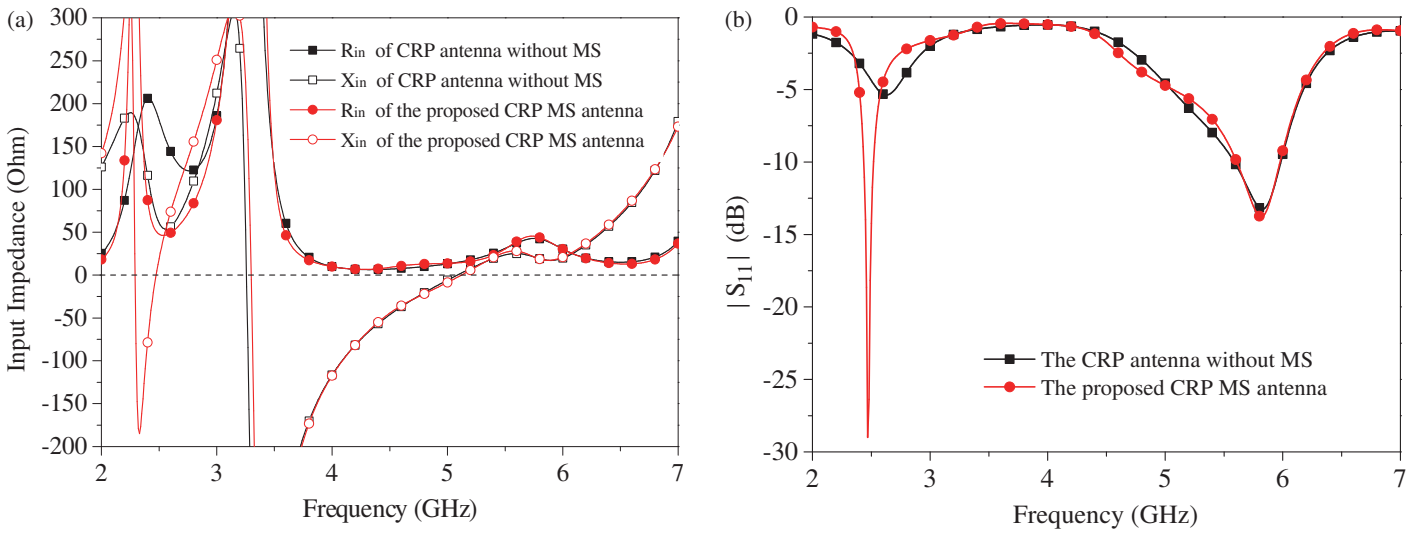

FIGURE 8. Simulated (a) input impedance and (b) $|S_{11}|$ of the antennas.

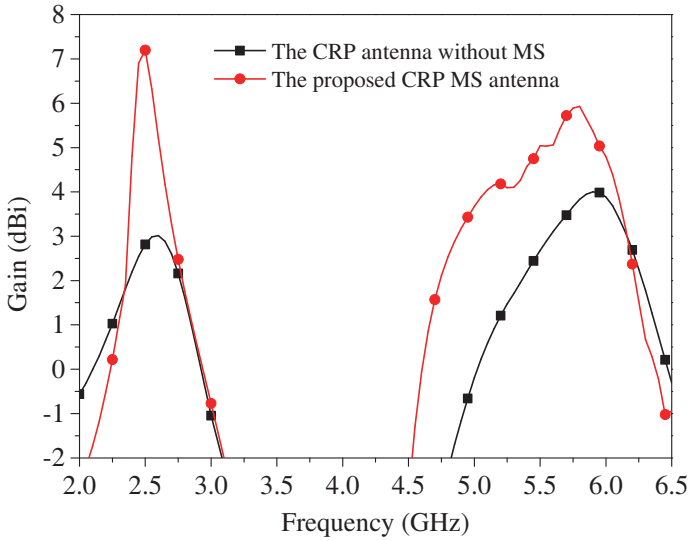

FIGURE 9. Simulated gains of the antennas without and with MS.

back of the CRP antenna to improve the impedance matching of the antenna in the lower band without affecting the upper band.

Next, Fig. 9 shows the simulated gains. For the CRP antenna without dual-cap MS, in the two operating bands, the peak gains of 3 and 4 dBi are obtained at 2.6 and 5.9 GHz, respectively. When the MS is introduced, the gain in the lower band is obviously improved, and the maximum gain reaches 7.19 dBi. Also, in the upper band, the gain is also enhanced and larger than 5 dBi. The peak gain reaches 6 dBi at 5.75 GHz.

In order to explain the reason for gain improvement, Fig. 10 gives the electric field distribution of the antennas at 2.47 and 5.82 GHz in the yoz plane. When the dual-cap MS has not been introduced, the energy is mainly concentrated near CRP, which leads to the lower gains at these two frequencies. When the MS is arranged as a reflector, the energy from the CRP is effectively reflected by the MS. As displayed in Fig. 2(b), the reflection phases of the MS unit are close to 125° and 100° at 2.47 and 5.82 GHz, respectively. The large reflection phase will lead to a large phase difference between the reflected wave and forward propagating wave when the distance between the CRP radiator and the MS is small. In this case, these two waves will be in a state of antiphase superposition state, and the field will be weakened. In order to enhance the superposition of two fields, the distance between the radiator and the MS is increased, which makes the phase difference between these two waves close to 0°. At this point, the total energy is enhanced, and the gain of the antenna is improved. Moreover, an induced current is generated on the dual-cap MS after the CRP is excited, and the effective radiation aperture of the antenna is enlarged. This also results in an increase in gain.

3.2. Parametric Study

In this section, the numerical analysis for the CRP MS antenna is made using HFSS. The results indicate that the parameters

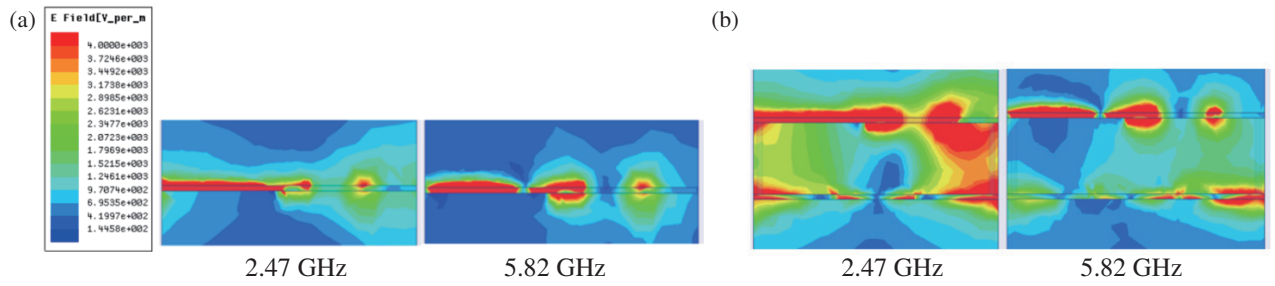

FIGURE 10. Simulated Electric field distribution of the antennas (a) without and (b) with MS in the yoz plane.

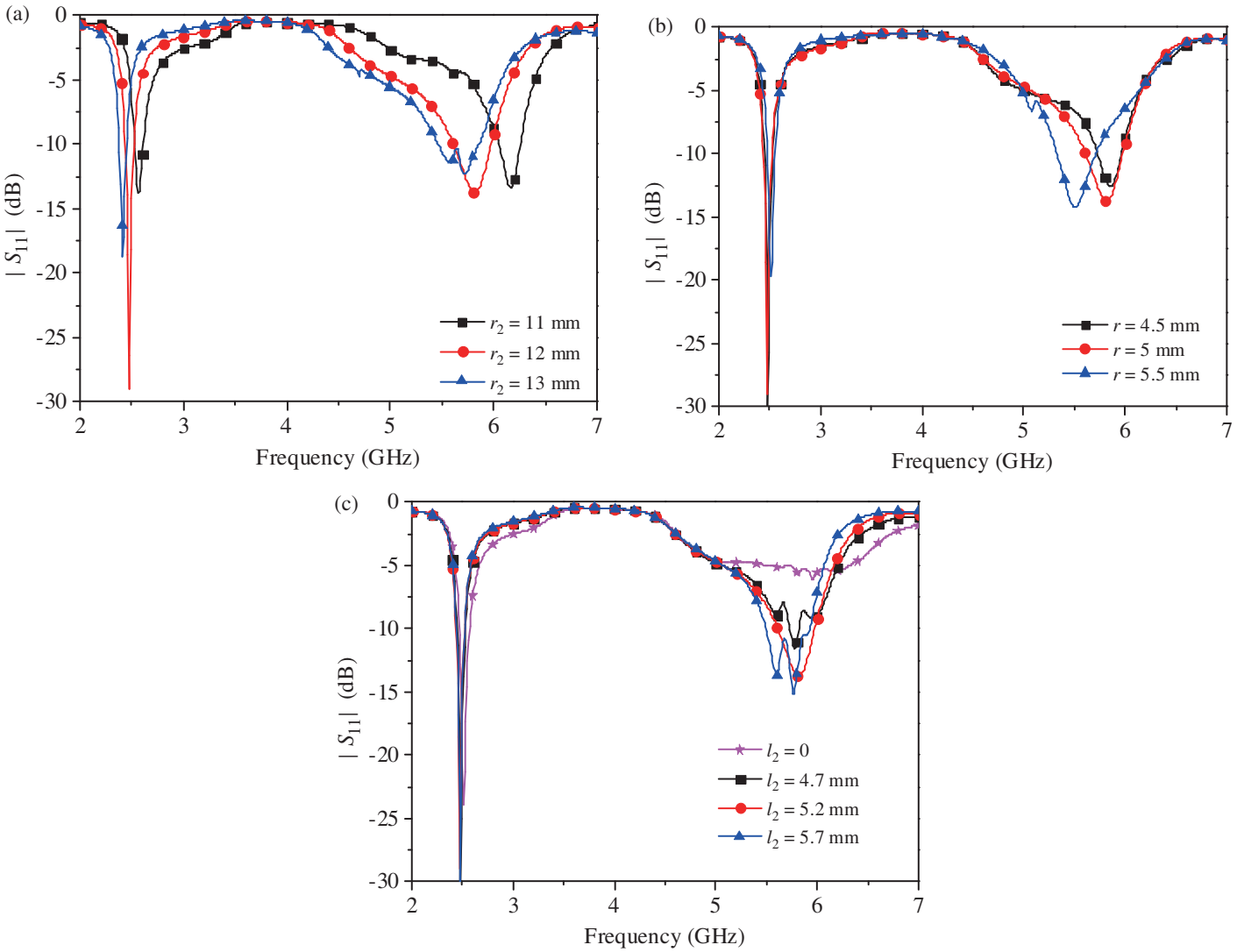

FIGURE 11. Simulated $|S_{11}|$ of the CRP MS antenna: (a) for different r_2, (b) for different r, and (c) for different l_2.

r_2, l_2 and r affect the performance of the antenna significantly. Fig. 11(a) shows the $|S_{11}|$ for different r_2. With the increase of r_2, the resonant frequencies both in the lower and upper bands shift down. When r_2 increases from 11 to 13 mm, the resonant frequencies decrease from 2.56 to 2.41 GHz and 6.16 to 5.71 GHz, respectively.

Figure 11(b) shows the $|S_{11}|$ for different r. It is observed that r mainly affects the impedance performance on the upper band. The impedance bandwidths of the lower band are almost unchanged with the increase of r. However, the resonant frequency in the upper band shifts down, and the bandwidth is broadened.

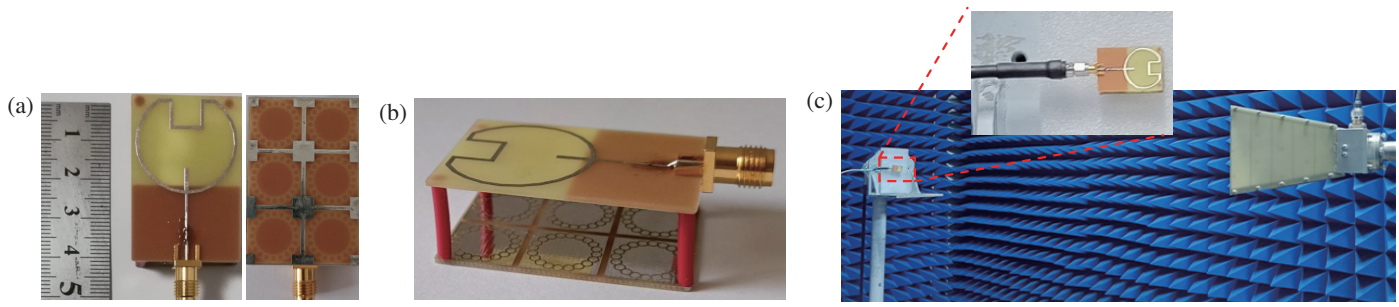

FIGURE 12. Photos of the proposed antenna and test environment: (a) top and bottom view, (b) side view, and (c) experimental environment.

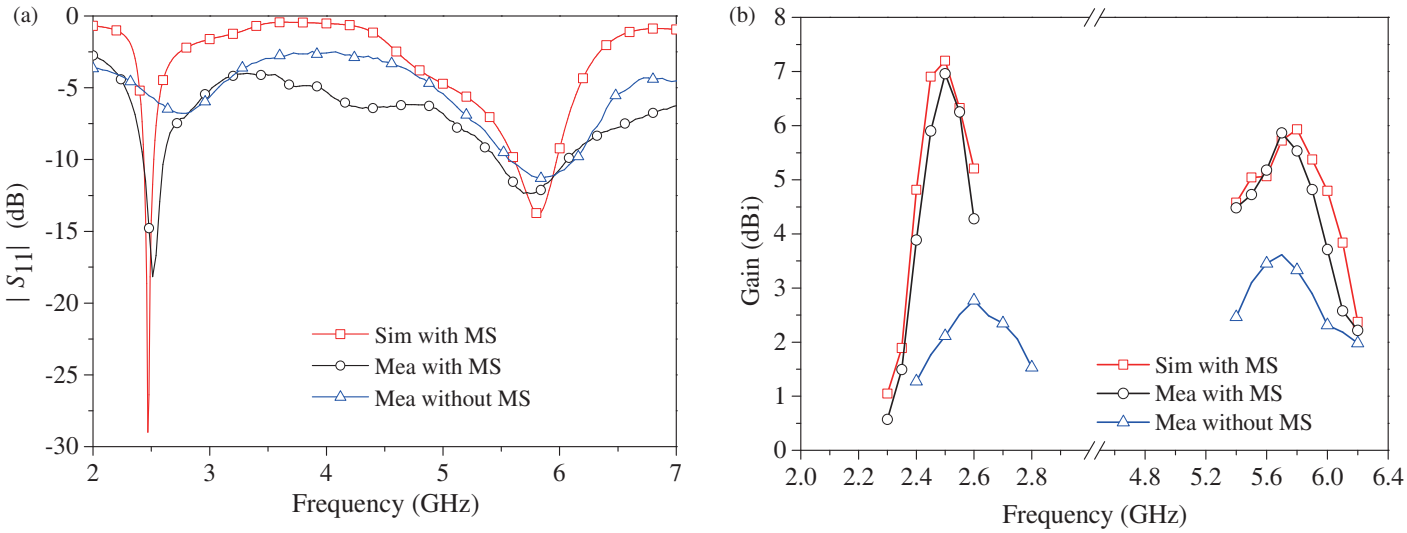

FIGURE 13. Simulated and measured results of the proposed antenna: (a) $|S_{11}|$ and (b) gain.

Figure 11(c) shows the $|S_{11}|$ for different l_2. It is observed that l_2 has little effect on $|S_{11}|$ in the lower band. Nevertheless, when the rectangular stub has not been introduced ($l_2 = 0$), the $|S_{11}|$ exceeds -10 dB in the upper band. When l_2 is 4.7 mm, a narrow operating band of 5.73–5.81 GHz is observed. After l_2 increases to 5.2 mm, a better impedance matching is obtained in a wider band of 5.6–5.98 GHz. However, the resonant frequency shifts down with the further increase of l_2. Also, the $|S_{11}|$ at 5.68 GHz is larger and close to -10 dB. Thus, $r_2 = 12$ mm, $r = 5$ mm, and $l_2 = 5.2$ mm are chosen, and the operating bands of the antenna are from 2.43 to 2.52 GHz and 5.6 to 5.98 GHz, respectively

4. SIMULATED AND MEASURED RESULTS

The proposed CRP MS antenna is fabricated. Figs. 12(a) and (b) show its photographs. Four thin nylon posts are used to bond the CRP radiator and MS. In order to reduce the impact on antenna performance, these nylon posts are placed on the four corners of the proposed CRP MS antenna without touching the circumferential circular ring slots loaded on the upper layer of MS. Moreover, Fig. 12(c) gives the test environment of the antenna. The ZVL13 vector network analyzer and SZ-VL antenna automatic test system are used to measure the antenna, and the results are shown in Figs. 13 and 14.

Figure 13(a) shows the simulated and measured $|S_{11}|$. When the MS has not been introduced, a poor impedance matching is achieved around 2.5 GHz band. Then, the dual-cap MS is arranged, and the antenna has the measured -10-dB impedance bandwidths of 170 MHz (2.43–2.6 GHz) and 570 MHz (5.48–6.05 GHz), which is better than the simulated result. This may be caused by the instability of the actual FR4-epoxy substrate. The permittivity of it may vary with frequency, and the loss may be larger than that in the simulation model. Fabrication and assembly tolerances also result in the deviation.

Figure 13(b) shows the gains of the antennas. For the antenna with dual-cap MS, in the lower and upper bands, the measured gains are stable and better than 4.2 dBi and 3.7 dBi, respectively. The peak gains of 6.9 and 5.8 dBi are obtained, which are improved by 4.8 and 2.3 dB compared to the antenna without MS at 2.5 and 5.7 GHz, respectively. It can be seen that the measured gain is less than the simulated one (7.19 and 6 dBi). This might be caused by the fabrication error.

Figure 14 shows the normalized radiation patterns at 2.47 and 5.82 GHz. Compared to the antenna without dual-cap MS, the one with MS has higher radiation along the boresight direction. In addition, it can be seen that the measured results agree well with the simulated ones. The maximum radiation is along the boresight direction. At 2.47 GHz, the half-power beamwidths

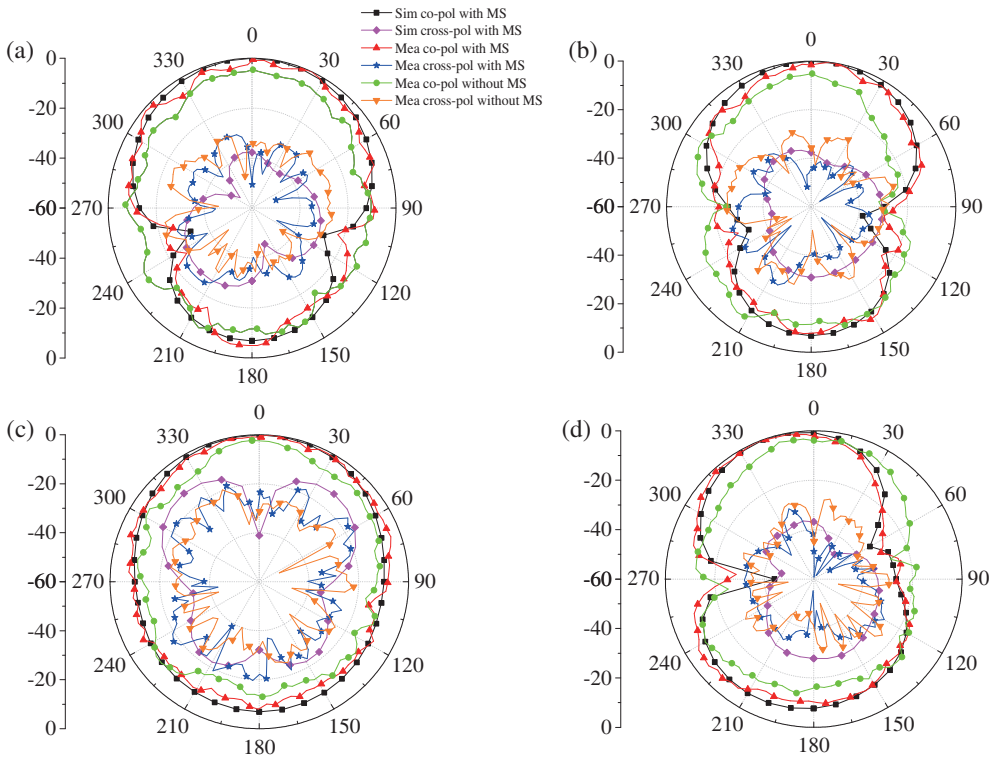

FIGURE 14. Simulated and measured radiation patterns: (a) E-plane at 2.47 GHz, (b) H-plane at 2.47 GHz, (c) E-plane at 5.82 GHz, and (d) H-plane at 5.82 GHz.

TABLE 2. Comparison of dual-band MS antennas.

	Dimension	Freq. (GHz)	BW (%)	Peak gain (dBi)
Ref. [14]	$2.7\lambda_0 \times 2.7\lambda_0 \times 0.11\lambda_0$	2.7/4.3	1/6.3	5/6.6
Ref. [15]	$0.58\lambda_0 \times 0.58\lambda_0 \times 0.058\lambda_0$	12/16.4	22.6/13.4	6.7/6.8
Ref. [16]	$0.38\lambda_0 \times 0.56\lambda_0 \times 0.1\lambda_0$	5.5/19.2	6.2/14.9	5.04/9.13
Ref. [17]	$1.2\lambda_0 \times 1.2\lambda_0 \times 0.057\lambda_0$	2.4/5.8	3.5/4.8	3.58/6.08
Ref. [18]	$0.45\lambda_0 \times 0.45\lambda_0 \times 0.02\lambda_0$	1.575/2.45	7.6/5.5	1.98/1.94
Ref. [19]	$0.68\lambda_0 \times 0.68\lambda_0 \times 0.053\lambda_0$	1.58/2.44	1.84/0.736	5.1/5.03
This work	$0.32\lambda_0 \times 0.21\lambda_0 \times 0.11\lambda_0$	2.52/5.8	6.76/9.9	6.9/5.8

λ_0, wavelength at the center frequency of the lower band. BW, impedance bandwidth.

are 90° and 55° in the E-plane and H-plane, respectively. Also, the cross-polarization radiation levels are both less than −20 dB. At 5.82 GHz, the half-power beamwidths are 70° and 55° in the two planes, respectively. In addition, although the cross-polarization radiation in E-plane is larger, it is still less than −30 dB in the boresight direction.

Finally, Table 2 lists the key data of dual-band MS antenna in this study and those reported in [14–19]. It can be seen that the proposed antenna has the minimum size and wide impedance bandwidth (except the ones in [15] and [16]). In addition, the peak gain of the proposed antenna is similar to those designs listed in Table 2.

5. CONCLUSION

A dual-band antenna based on dual-cap MS is designed and realized in this paper. By introducing LCS and PCCRS, the dimensions of the MS are reduced. Meanwhile, the dual-band operation is provided. In addition, as a reflector, the dual-cap MS is placed at the back of the CRP antenna for performance enhancement. The results confirm that the dual-band CRP MS antenna has a total volume of $0.32\lambda_0 \times 0.21\lambda_0 \times 0.11\lambda_0$ (at 2.47 GHz), and its impedance matching in lower band is improved. Also, the boresight gains over the two operation frequency bands (2.43–2.6 GHz and 5.48–6.05 GHz) are obviously improved, up to 6.9 and 5.8 dBi, respectively. It is suitable for wireless interconnection of electrical equipment in indoor environments in the WLAN frequency band, such as dual-band wireless routers and dual-band RFID antennas.

ACKNOWLEDGEMENT

This work was supported by the Fundamental Research Program of Shanxi Province of China (202203021221215).

REFERENCES

[1] Cai, T., G.-M. Wang, X.-F. Zhang, and J.-P. Shi, "Low-profile compact circularly-polarized antenna based on fractal metasurface and fractal resonator," *IEEE Antennas and Wireless Propagation Letters*, Vol. 14, 1072–1076, 2015.

[2] Zhao, Y., X. Cao, J. Gao, X. Yao, and X. Liu, "A low-RCS and high-gain slot antenna using broadband metasurface," *IEEE Antennas and Wireless Propagation Letters*, Vol. 15, 290–293, 2015.

[3] Cao, Y. F., S. W. Cheung, and T. I. Yuk, "Dual-cap mushroom-like metasurface used in CP reconfigurable monopole antenna for performance enhancement," *IEEE Transactions on Antennas and Propagation*, Vol. 63, No. 12, 5949–5955, 2015.

[4] Feng, G., L. Chen, X. Xue, and X. Shi, "Broadband surface-wave antenna with a novel nonuniform tapered metasurface," *IEEE Antennas and Wireless Propagation Letters*, Vol. 16, 2902–2905, 2017.

[5] Nie, N.-S., X.-S. Yang, Z. N. Chen, and B.-Z. Wang, "A low-profile wideband hybrid metasurface antenna array for 5G and WiFi systems," *IEEE Transactions on Antennas and Propagation*, Vol. 68, No. 2, 665–671, 2020.

[6] Zhu, H. L., S. W. Cheung, and T. I. Yuk, "Mechanically pattern reconfigurable antenna using metasurface," *IET Microwaves, Antennas & Propagation*, Vol. 9, No. 12, 1331–1336, 2015.

[7] Xu, P., W. X. Jiang, X. Cai, S. H. Bai, and T. J. Cui, "An integrated coding-metasurface-based array antenna," *IEEE Transactions on Antennas and Propagation*, Vol. 68, No. 2, 891–899, 2020.

[8] Chen, J., W. Yuan, C. Zhang, W. X. Tang, L. Wang, Q. Cheng, and T. J. Cui, "Wideband leaky-wave antennas loaded with gradient metasurface for fixed-beam radiations with customized tilting angles," *IEEE Transactions on Antennas and Propagation*, Vol. 68, No. 1, 161–170, 2020.

[9] Liu, F., J. Guo, L. Zhao, G.-L. Huang, Y. Li, and Y. Yin, "Dual-band metasurface-based decoupling method for two closely packed dual-band antennas," *IEEE Transactions on Antennas and Propagation*, Vol. 68, No. 1, 552–557, 2020.

[10] Ahmed, A., M. R. Robel, and W. S. T. Rowe, "Dual-band two-sided beam generation utilizing an EBG-based periodically modulated metasurface," *IEEE Transactions on Antennas and Propagation*, Vol. 68, No. 4, 3307–3312, 2020.

[11] Zheng, Q., J. Wang, P. PourMohammadi, and X. Pang, "Dual-band metasurface-based closely packed antennas by controlling surface wave propagation," *IEEE Antennas and Wireless Propagation Letters*, Vol. 23, No. 5, 1633–1637, 2024.

[12] Fan, Y., Y. Cheng, and Y. Dong, "A wideband shared-aperture dual-band base-station antenna array based on inhomogeneous metasurface," *IEEE Antennas and Wireless Propagation Letters*, Vol. 23, No. 2, 463–467, 2024.

[13] Sahu, N. K. and S. K. Mishra, "Polarization-converting metasurface inspired dual-band dual-circularly polarized monopole antennas for off-body communications," *IEEE Antennas and Wireless Propagation Letters*, Vol. 22, No. 1, 194–198, 2023.

[14] Kumar, G., B. Ghosh, V. K. Singh, and M. B. Mahajan, "Dual band metasurface polarizer for LP to CP conversion," in *2023 IEEE Microwaves, Antennas, and Propagation Conference (MAPCON)*, 1–5, Ahmedabad, India, 2023.

[15] Gu, Y., X.-X. Yang, T. Lou, and Y. Wu, "Low-profile dual-band magneto-electric dipole antenna loaded with metasurface," *IEEE Antennas and Wireless Propagation Letters*, Vol. 21, No. 7, 1492–1496, 2022.

[16] Asif, M., D. A. Sehrai, S. H. Kiani, J. Khan, M. Abdullah, M. Ibrar, M. Alibakhshikenari, F. Falcone, and E. Limiti, "Design of a dual band SNG metamaterial based antenna for LTE 46/WLAN and Ka-band applications," *IEEE Access*, Vol. 9, 71 553–71 562, 2021.

[17] Ramli, M. N., P. J. Soh, M. F. Jamlos, H. Lago, N. M. Aziz, and A. A. Al-Hadi, "Dual-band wearable fluidic antenna with metasurface embedded in a PDMS substrate," *Applied Physics A*, Vol. 123, 149, 2017.

[18] Joshi, R., E. F. N. M. Hussin, P. J. Soh, M. F. Jamlos, H. Lago, A. A. Al-Hadi, and S. K. Podilchak, "Dual-band, dual-sense textile antenna with AMC backing for localization using GPS and WBAN/WLAN," *IEEE Access*, Vol. 8, 89 468–89 478, 2020.

[19] Paracha, K. N., S. K. A. Rahim, P. J. Soh, M. R. Kamarudin, K.-G. Tan, Y. C. Lo, and M. T. Islam, "A low profile, dual-band, dual polarized antenna for indoor/outdoor wearable application," *IEEE Access*, Vol. 7, 33 277–33 288, 2019.

[20] Faeghi, P., C. Ghobadi, J. Nourinia, and B. Virdee, "Nanoparticle-coated vivaldi antenna array for gain enhancement," *Applied Physics A*, Vol. 129, No. 3, 217, 2023.

[21] Chen, X., T. M. Grzegorczyk, B.-I. Wu, J. P. Jr, and J. A. Kong, "Robust method to retrieve the constitutive effective parameters of metamaterials," *Physical Review E*, Vol. 70, No. 1, 016608, 2004.